Study on Dual-Frequency Imaging of Capacitively Coupled Electrical Impedance Tomography: Frequency Optimization

Yandan Jiang, Junchao Huang, Haifeng Ji, Baoliang Wang*, Zhiyao Huang and Manuchehr Soleimani

***Abstract*—In this work, a new dual-frequency imaging framework of capacitively coupled electrical impedance tomography (CCEIT) is presented. Unlike conventional single-frequency imaging, the dual-frequency imaging adopts two different working frequencies to obtain the real part and the imaginary part of the impedance respectively. With the real part image and the imaginary part image at the two frequencies, the framework further introduces image fusion to obtain the fused image. This work focuses on optimization of the two working frequencies. To achieve the optimal selection of the two frequencies, data collection in a wide range frequency is carried out. The multifrequency data is then analyzed in depth and investigated from several aspects, including the measurement data, the sensitivity distribution and the imaging quality. Experiment was carried out with a 12-electrode CCEIT sensor, an impedance analyzer, and a computer to obtain the real part and imaginary part measurements of the impedance. Research results show that a low working frequency is recommended for the real part, while a relatively high working frequency is recommended for the imaginary part. Within the investigated frequency range of 200 kHz - 20 MHz, the optimized frequencies for the real part and the imaginary part are 1 MHz and 15 MHz respectively. Results of verification experiment shows the superior performance of the two selected frequencies. Additionally, this paper demonstrates the advantages of the dual-frequency imaging framework. Compared with CCEIT in individual frequencies, CCEIT based on dual-frequency imaging with the two optimized frequencies has much better imaging performance.**

***Index Terms*—Electrical impedance tomography (EIT), capacitively coupled electrical impedance tomography (CCEIT), dual-frequency imaging, working frequency**

I. INTRODUCTION

WITH the advantages of low cost, high speed, simple structure and no radiation, electrical impedance tomography (EIT) has become a widely accepted technique for distribution reconstruction of conductive medium, which is applicable in both industrial processes and biomedical cases [1-5]. But, there still exist some issues limiting its practical applications. One problem of traditional EIT is its contact measurement principle. The contact between the electrodes and the measured medium has some unfavorable effects, such as electrochemical erosion, polarization effect and electrode contamination, which is more prominent in practical industrial applications [2, 6-8], and contact impedance which is notable in biomedical applications [9, 10]. Another problem of EIT is the inadequate usage of impedance information. Traditional EIT usually uses the real part or the amplitude of the impedance for imaging, and EIT-related works, which pay attention to the whole impedance information of the measured medium, especially the imaginary part, are very limited [3-5].

Capacitively coupled electrical impedance tomography (CCEIT) is a new modality of electrical tomography (ET), which provides an approach to overcome the two mentioned problems of EIT [11, 12]. In CCEIT, the capacitively coupling idea is introduced to implement contactless measurement of the medium impedance in the region of interest (ROI), and both the real part and the imaginary part of the impedance are used for imaging. Although previous research has verified that combining the real part and the imaginary part by image fusion is an effective way to improve the imaging performance, the current CCEIT system is based on single-frequency imaging, i.e., the real part and the imaginary part of the impedance are obtained at the same frequency. It is found that the two parts of the impedance have different spectral characteristics, which means it is difficult to seek a frequency that works satisfactory for both the two parts [13-15]. Besides, some pioneering researches have indicated that multi-frequency imaging can give a better insight into the medium distribution in ROI and obtain inspiring result with traditional ET [16-18]. The idea of multi-frequency imaging provides a possible approach to improve the CCEIT technique. To make better use of the impedance information obtained by CCEIT, the relationships between the two parts of impedance and frequency should be investigated separately, especially the imaginary part which has high frequency dependence. So, more corresponding research with CCEIT should be undertaken.

This work was supported in part by the National Natural Science Foundation of China under Grant 51976189. *(Corresponding author: Baoliang Wang).*

Yandan Jiang, Junchao Huang, Haifeng Ji, Baoliang Wang, Zhiyao Huang are with the State Key Laboratory of Industrial Control Technology, College of Control Science and Engineering, Zhejiang University, Hangzhou 310027, China (e-mail: ydjiang@zju.edu.cn; jc_huang@zju.edu.cn; hfji@zju.edu.cn; wangbl@zju.edu.cn; zy_huang@zju.edu.cn).

Manuchehr Soleimani is with the Engineering Tomography Laboratory (ETL), Department of Electronic and Electrical Engineering, University of Bath, Bath BA2 7AY, UK (e-mail: M.Soleimani@bath.ac.uk).

Color versions of one or more of the figures in this article are available online at http://ieeexplore.ieee.org

This work proposes a dual-frequency imaging framework of CCEIT and focuses on optimization of the two working frequencies based on this framework. Three aspects, including the measurement data, the sensitivity distribution and the imaging quality, are investigated and compared to select the most effective working frequencies for the real part and the imaginary part of the impedance. Simulation will be undertaken to calculate the sensitivity matrices and experiments with different distributions in ROI will be carried out to obtain the impedance measurements. In verification experiment, imaging results obtained by dual-frequency imaging with the two optimized working frequencies will be compared with images obtained at a series of individual frequencies to verify the effectiveness of dual-frequency imaging and the two optimized frequencies.

II. Dual-Frequency Imaging Framework

As aforementioned, compared with traditional EIT, CCEIT makes two improvements. One is implementing contactless impedance measurement by introducing the capacitively coupling idea, the other is regarding the measured medium as an impedance and uses both the real and imaginary parts [11, 12].

Fig.1 shows the measurement principle of CCEIT. In CCEIT sensor, the electrodes are evenly attached to the outer wall of the insulation pipe, forming a ring-shaped sensing array. According to capacitively coupling idea, for each electrode, a coupling capacitance will be formed by the electrode, the insulation pipe and the conductive medium in ROI. During measurement, one electrode will be selected as the excitation electrode and another electrode will be selected as the detection electrode, while other electrodes will be at floating potential. Fig. 1(b) is the equivalent circuit of a measurement electrode pair, where C_1, C_2 are the two coupling capacitances and Z_x is the equivalent impedance of the measured medium between the two electrodes. When an excitation AC voltage source is applied to the excitation electrode, an output current can be obtained at the detection electrode for impedance calculation. By switching the measurement electrode pair, 66 independent impedance measurements will be obtained with the 12-electrode CCEIT sensor, including 66 real part measurements and 66 imaginary part measurement.

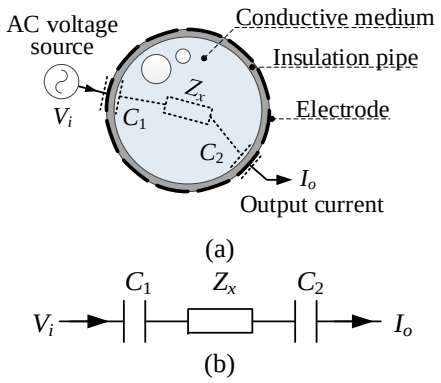

Fig. 1 Measurement principle of CCEIT: (a) 12-electrode sensor; (b) Equivalent circuit of a measurement electrode pair.

The ROI of a working CCEIT sensor can be regarded as a quasi-static electromagnetic field, which satisfies the following model with the frequency of the AC voltage source f [11, 12]:

$$\nabla\cdot((\sigma(x,y)+j\omega\varepsilon(x,y))\nabla\varphi(x,y))=0 \quad (x,y)\subseteq\Omega \qquad (1)$$

where $\sigma(x, y)$, $\varepsilon(x, y)$ and $\varphi(x, y)$ are the spatial conductivity, permittivity and potential distributions in the ROI Ω, respectively. $\omega=2\pi f$ is the angular frequency of the AC voltage source, with the frequency f.

According to the measurement strategy, the boundary conditions of Equation (1) are:

$$\begin{cases}\varphi_a(x,y)=V & (x,y)\subseteq\Gamma_a\\ \varphi_b(x,y)=0 & (x,y)\subseteq\Gamma_b\\ \partial\varphi_c(x,y)/\partial\vec{n}=0 & (x,y)\subseteq\Gamma_c,(c\neq a,b)\end{cases} \qquad (2)$$

where a, b and c stand for the excitation electrode, the detection electrode and the floating electrode(s) categories respectively. So, $\varphi_a(x, y)$, $\varphi_b(x, y)$, $\varphi_c(x, y)$ and Γ_a, Γ_b, Γ_c represent the potentials and the spatial regions of the excitation electrode, the detection electrode and the floating electrode(s) respectively. V is the amplitude of the excitation AC voltage source. $\vec{n}$ denotes the outward unit normal vector.

Generally, the interested impedance Z_x can be equivalent to the parallel of a resistance R_{x1} and a capacitance C_x in series with a resistance R_{x2}, as shown in Fig. 2 [1, 2]. Then, Z_x can be described as

$$Z_x=R+jX=\left(\frac{R_{x1}}{1+\omega^2C_x^2R_{x1}^2}+R_{x2}\right)+j\left(-\frac{\omega C_xR_{x1}}{1+\omega^2C_x^2R_{x1}^2}\right) \qquad (3)$$

where R is the real part of the impedance and X is the imaginary part of the impedance.

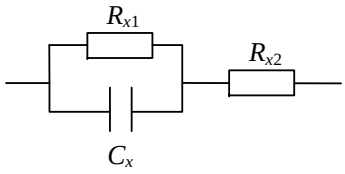

Fig. 2 Detailed equivalent circuit of a measurement electrode pair.

Traditional EIT uses the amplitude of the measured impedance for imaging in most cases, where the real part and the imaginary part are utilized in a combined version. CCEIT regards the two parts as two kinds of impedance information and uses them for separate image reconstruction. However, previous CCEIT system is based on single-frequency imaging, where the real part and the imaginary part used for imaging are obtained at the same frequency. As can be seen from Eq. (3), the two parts have different spectral characteristics. Compared with the real part, the imaginary part is more frequency-dependent. From the measurement aspect, different frequency correlations indicate that the highest signal-to-noise ratio (SNR) of the real part measurements and imaginary part measurements will be obtained at different frequencies. So, using the same working frequency to obtain them is not a good idea. Different working frequencies should be adopted for the measurement of the real part and the imaginary part of the impedance.

Based on the above consideration, a dual-frequency imaging framework is proposed in this work. Fig. 3 shows the proposed framework, where two different working frequencies are adopted to obtain the real part and the imaginary part of the impedance respectively. With the measurements of the two parts obtained at the two frequencies, image reconstruction is implemented to obtain the real part image and the imaginary part image. Then, image fusion is introduced to fuse the two images and obtain the fused image.

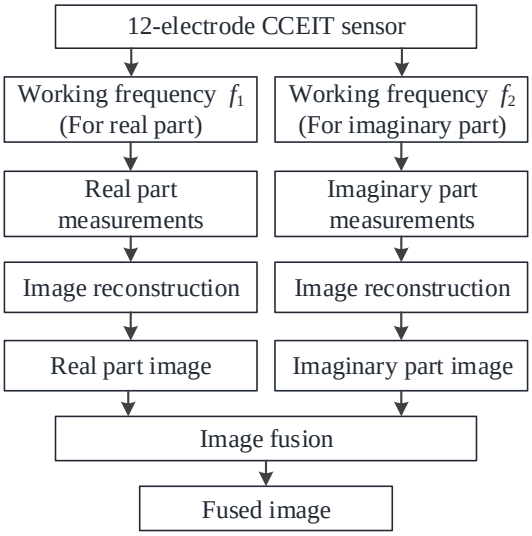

Fig. 3. The dual-frequency imaging framework.

In the dual-frequency imaging framework, the selection of the two frequencies are the most critical point. So seeking the optimal working frequencies for the real part and the imaginary part is the main focus of this work. To implement this, the performance of CCEIT in a wide frequency range is to be evaluated. Fig.4 shows the experimental setup, which includes a 12-electrode CCEIT sensor, an impedance analyzer and a personal computer. The CCEIT sensor consists of an insulation pipe and the 12 electrodes. Table I lists the detailed information of the sensor. The impedance analyzer (Keysight 4294A) is used to obtain the impedance measurements in a wide frequency range of 200 kHz - 20 MHz. The computer is used for data processing and image reconstruction. Fig.5 is a photo of the experimental setup.

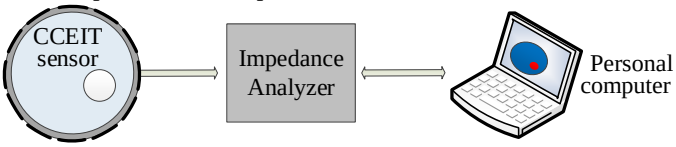

Fig. 4 The experimental setup.

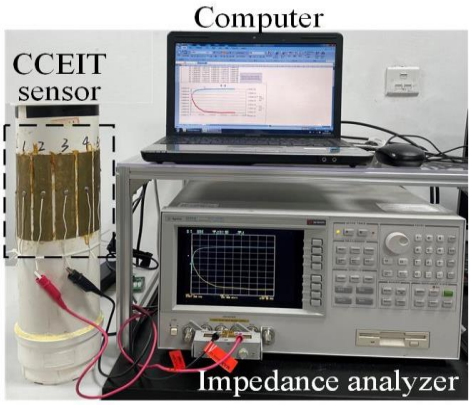

Fig. 5 A photo of the experimental setup.

TABLE I
DETAILS OF THE CCEIT SENSOR

Insulation pipe	Material	Polyvinyl chloride
	Inner diameter	106 mm
	Outer diameter	110 mm
Electrodes	Material	Copper foil
	Length	150 mm
	Width	24 mm

III. WORKING FREQUENCY OPTIMIZATION

In the idea of dual-frequency imaging, selection of the two working frequencies is the most significant step. In this work, three aspects of CCEIT in a wide frequency range of 200 kHz - 20 MHz are evaluated to seek the most effective frequencies for the two parts, including the measurement data (the projection), the sensitivity distribution and the imaging quality.

With the experimental setup, experiments were carried out to investigate the relationship between the two parts of impedance and the frequency. Fig. 6 shows the three distribution setups S1 - S3 for frequency selection investigation, where tap water (σ_1 = 0.012 S/m, ε_1 = 78) and plastic rod(s) (σ_2 = 0 S/m, ε_2 = 3) with the diameter of 29.5 mm are used to simulate the background medium and the target medium, respectively.

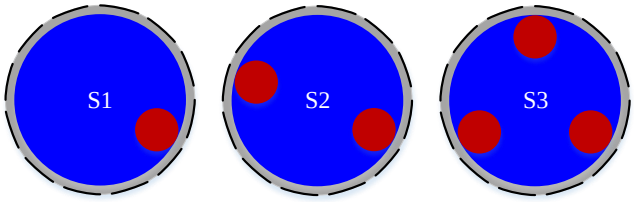

Fig. 6 Distribution setups for frequency selection.

A. Measurement Data

At each frequenccy, with the impedance measurements (the real part measurements and the imaginary part measurements) obtained by the impedance analyzer, the real part projections and the imaginary part projections can be calculated as:

$$p_m^R = \frac{R_m - R_m^0}{R_m^0} \tag{4}$$

$$p_m^X = \frac{X_m - X_m^0}{X_m^0} \quad (5)$$

where, p_m^R and p_m^X are the mth real part projection and imaginary part projection calculated respectively by the mth real part measurement R_m and imaginary part measurement X_m, m = 1, 2, …, M and M is the number of independent measurements. For the 12-electrode CCEIT sensor, M = 66.

From the measurement aspect, 37 frequency points in the frequency range of 200 kHz - 20MHz are investigated. At each frequenccy, two groups of the impedance measurements, one is the real part measurement group and the other is the imaginary part measurement group, are obtained by the impedance analyzer. Correspondingly, the real part projection group and the imaginary part projection group can be calculated.

Fig. 7 shows the impedance measurements obtained by the impedance analyzer and the calculated projections, where the blue curves represent the real part and the orange curves represent the imaginary part. Every point in the curves is the average of the 66 independent measurements/projections in one group (the real part measurement/projection group or the imaginary part measurement/projection group). Fig. 7(a) shows how the average value of impedance measurements changes with frequency. The solid line represents the background measurement, which is obtained when the ROI is filled with background medium, and the dotted line represents the average measurement with the distribution setups in Fig. 6. Whether there exists target medum or not, as the frequency goes up, the real part measurement decreases, while the imaginary part measurement increases. Fig. 7(b) shows the relationship between the average value of real/imaginary part projections and the frequency. An overall downward trend can be observed in the real part projection with the increase of frequency, but it is intersting to find that there is a peak around 1 MHz. And for the imaginary part, the average projection goes up with frequency.

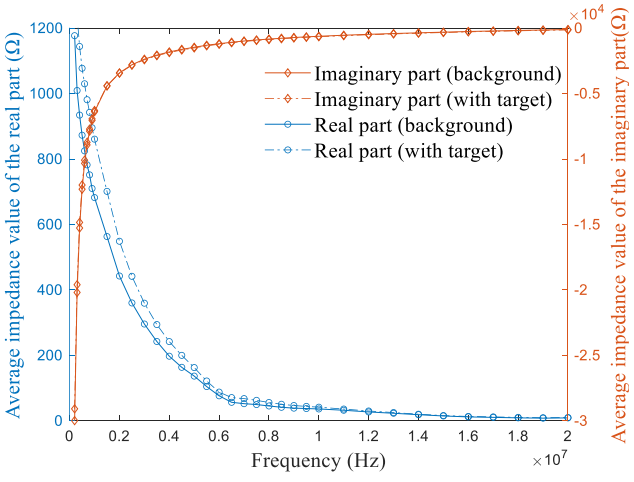

(a)

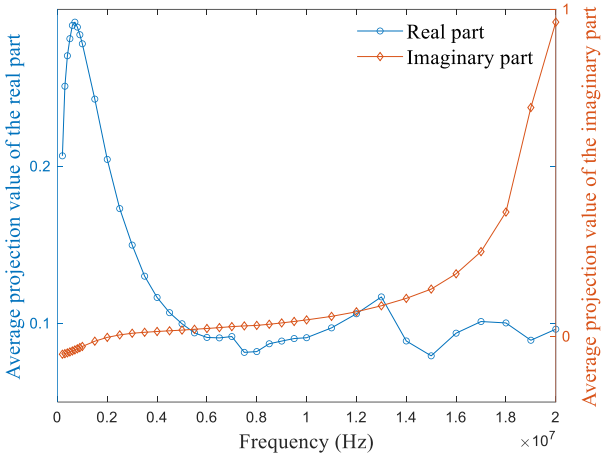

(b)

Fig. 7 Impedance measurements and projections of CCEIT in the investigated frequency range: (a) Average impedance measurement; (b) Average projection.

B. Sensitivity Distribution

Calculation of the sensitivity matrix is a significant part in tomography. Sensitivity matrix is also called Jacobian matrix, which is a coefficient matrix mapping the relationship between the internal distribution in ROI (the image pixel vector) and the impedance measurements (the projection vector) [19]. Based on the finite element method (FEM), simulation by COMSOL Multiphysics and Matlab was carried out to calculate the real part sensitivity matrix and the imaginary part sensitivity matrix with the 12-electrode CCEIT setup. For the sensitivity $S = [s_{mn}]_{M\times N}$ (m = 1, 2, …, M, n = 1, 2, …, N), M is the number of independent measurements and N is the number of elements. Here. M = 66 for the 12-electrode CCEIT sensor and N = 1024 elements (32×32 squares) are meshed in FEM. In detail, the sensitivity which associates the real part of the mth impedance measurement with the nth element is defined as:

$$s_{mn}^R = \frac{R_{mn} - R_m^0}{R_m^0} \quad (6)$$

where R_m^0 is the real part the mth impedance measurement obtained when the pipe is filled with background medium ($\sigma = \sigma_1$, $\varepsilon = \varepsilon_1$) and R_{mn} is the imaginary part of the mth impedance measurement obtained when the nth element changes from the background medium to the target medium ($\sigma = \sigma_2$, $\varepsilon = \varepsilon_2$).

Similarly, the sensitivity that associates the imaginary part of the mth impedance measurement with the nth element s_{mn}^Xt is defined as:

$$s_{mn}^X = \frac{X_{mn} - X_m^0}{X_m^0} \quad (7)$$

where X_m^0 is the imaginary part of the mth impedance measurement obtained when the pipe is filled with background medium ($\sigma = \sigma_1$, $\varepsilon = \varepsilon_1$) and X_{mn} is the imaginary part of the mth impedance measurement obtained when the nth element changes from the background to target medium ($\sigma = \sigma_2$, $\varepsilon = \varepsilon_2$).

According to the definitions of sensitivity matrices, a pair of

sensitivity matrices (S^R and S^X) will be calculated for every investigated frequency point. For each part at each frequency, there are six typical sensitivity distributions representing six relative positions between the two electrodes in the measurement electrode pair, i.e., from the adjacent electrode pair to the opposite electrode pair. To make quantitative comparison, the average sensitivity S_a and the uniformity coefficient S_u of the typical sensitivity distributions are introduced, which are defined as [23, 24]:

$$S_a = \frac{1}{6}\sum_{k=1}^{6}\overline{s_k} \tag{8}$$

$$S_u = \frac{1}{6}\sum_{k=1}^{6}\frac{v_k}{\overline{s_k}} \tag{9}$$

where $\overline{s_k}$ and v_k are the mean and standard deviation of the sensitivities in the kth typical sensitivity distribution (the kth row of the sensitivity matrix) calculated by the following equations:

$$\overline{s_k} = \frac{1}{N}\sum_{n=1}^{N} s_{kn} \tag{10}$$

$$v_k = \sqrt{\frac{1}{N-1}\sum_{n=1}^{N}(s_{kn}-\overline{s_k})^2} \tag{11}$$

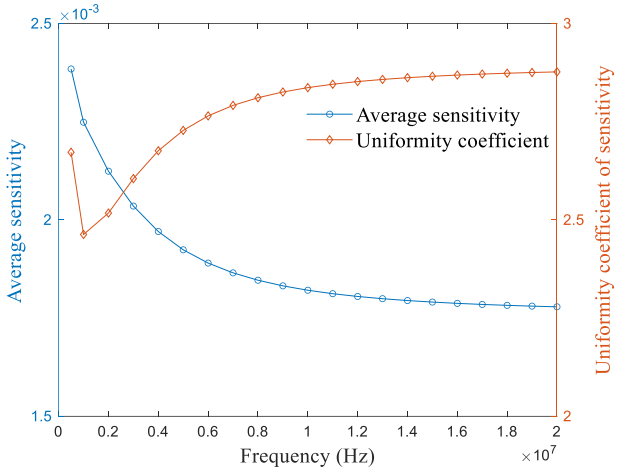

(a)

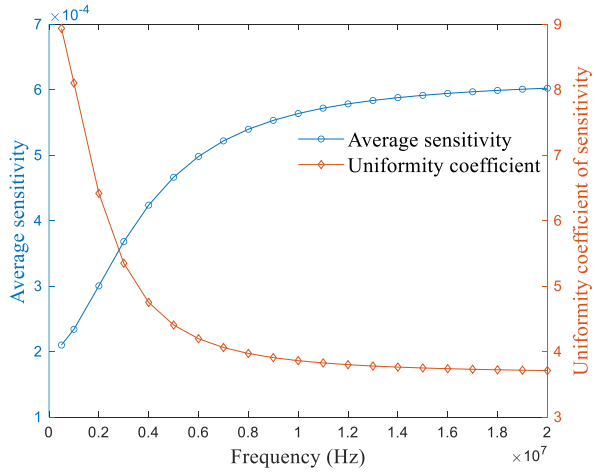

(b)

Fig. 8 Sensitivity distribution indexes of CCEIT in the investigated frequency range: (a) The real part; (b) The imaginary part.

The FEM-based simulation work to obtain the sensitivity matrices is quite time-consuming. In this part, sensitivity matrices at 21 frequency points in the frequency range of 200 kHz - 20 MHz are calculated by FEM simulation. Fig.8 shows the sensitivity distribution indexes of the typical sensitivity distributions of CCEIT in the investigated frequency range, where Fig. 8 (a) represents the two indexes of the real part sensitivity distribution and Fig.8 (b) represents the two indexes of the imaginary part sensitivity distribution. Generally, sensitivity distribution with higher average sensitivity and lower uniformity coefficient (more uniform) is considered to be better. As can be seen from Fig. 8(a), the average sensitivity decreases with the frequency increase and the uniformity coefficient increases with the frequency increase, indicating that the real part sensitivity distribution is better at lower frequency. But again 1 MHz attracts attention because the real part sensitivity distribution at 1 MHz is the most uniform. In Fig. 8(b), an opposite conclusion can be drawn. That is, better imaginary part sensitivity distribution can be obtained at higher frequency.

C. Imaging Quality

Image reconstruction is to reconstruct the image that reflects the medium distribution in ROI. Mathematically, it is to solve the following inverse problem [19-21]:

$$P = SG \tag{12}$$

where $P=[p_m]_{M\times 1}$ and $S=[s_{mn}]_{M\times N}$ are respectively the projection vector and previously defined sensitivity matrix. $G=[g_n]_{N\times 1}$ is the image pixel vector to be reconstructed. The real part projections and the imaginary part projections are defined as:

$$p_m^R = \frac{R_m - R_m^0}{R_m^0} \tag{13}$$

$$p_m^X = \frac{X_m - X_m^0}{X_m^0} \tag{14}$$

where, p_m^R and p_m^X are the mth real part projection and imaginary part projection calculated respectively by the mth real part measurement R_m and imaginary part measurement X_m.

In this work, the combination of linear back projection (.LBP) and Landweber iterative algorithms are used to implement image reconstruction. LBP is introduced to provide an initial solution to the inverse problem in Equation (5) (the original image gray vector $G^0=[g_n^0]_{N\times 1}$), which can be described as [19]:

$$g_n^0 = \frac{\sum_{m=1}^{M} p_m s_{mn}}{\sum_{m=1}^{M} s_{mn}} \tag{15}$$

Taken the initial solution in Equation (8) as the initial value of iteration, Landweber iterative algorithm is used to obtain a more accurate solution (the reconstructed image gray vector $G=[g_n]_{N\times 1}$). The idea of Landweber iterative can be described as

the following equation [20,21]:

$$g_n(k+1) = g_n(k) - \alpha \sum_{m=1}^{M} s_{mn}\left(p_m - \sum_{n=1}^{N} s_{mn} g_n(k)\right) \quad (16)$$

where α is the relaxation factor, which is a positive scalar. $g_n(k)$ and $g_n(k+1)$ are the kth and the $(k+1)$th iteration results of the nth element.

With the real part projection vector P^R and the real part sensitivity matrix S^R, the real part initial image G^R can be reconstructed by the LBP + Landweber method. Similarly, with the imaginary part projection vector P^X and the imaginary part sensitivity matrix S^X, the imaginary part initial image G^X can also be reconstructed by the LBP + Landweber method. To evaluate and compare the image quality of the real/imaginary part images reconstructed at different frequencies by LBP + Landweber iterative algorithm, the image relative error (*IRE*) and the image correlation coefficient (*ICC*) are introduced [25], which are defined as:

$$IRE = \sqrt{\frac{\sum_{n=1}^{N}(g_n - g_n^*)^2}{\sum_{n=1}^{N}(g_n^*)^2}} \quad (17)$$

$$ICC = \frac{\sum_{n=1}^{N}(g_n - g_a)(g_n^* - g_a^*)}{\sqrt{\sum_{n=1}^{N}(g_n - g_a)^2 \sum_{n=1}^{N}(g_n^* - g_a^*)^2}} \quad (18)$$

where $\tilde{G} = [\tilde{g}_n]_{N\times 1}$ and $G^*=[g_n^*]_{N\times 1}$ are the normalized reconstructed image gray vector to be evaluated and the actual image gray vector of the tested distribution. $\tilde{g}_a$ and g_a^* are respectively the average gray level of the reconstructed image and the average gray level of the actual image.

Fig.9 shows the image quality indexes of CCEIT in the investigated frequency range, where Fig. 9(a) is with the real part and Fig. 9(b) is with the imaginary part. Every point in the figure is the average index value of the three reconstructed distribution setups at the specified frequency.

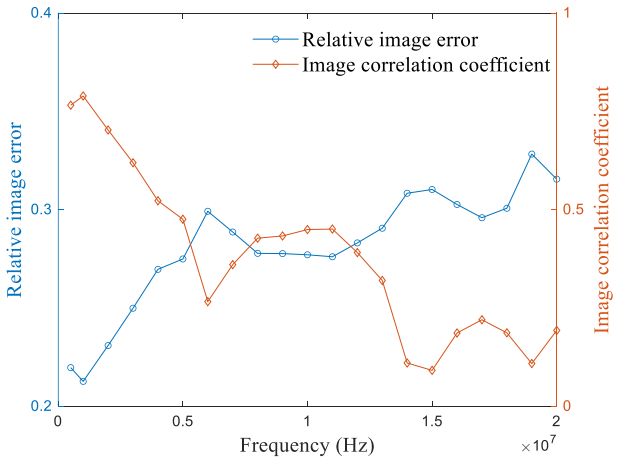

(a)

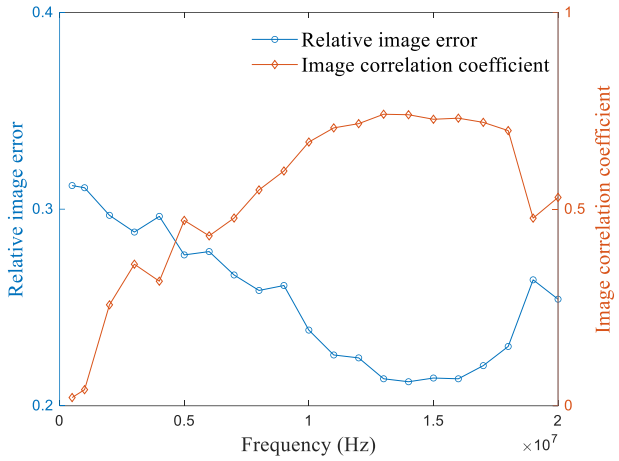

(b)

Fig. 9 Image quality indexes of CCEIT in the investigated frequency range: (a) The real part; (b) The imaginary part.

From Fig. 9, it is found that for the real part, the images reconstructed at low working frequency have better image quality than those reconstructed at higher working frequency, and both the smallest relative image error and the largest image correlation coefficient lie at 1 MHz. While for the imaginary part, as the frequency increases in the investigated range, the quality indexes show a positive trend before 13 MHz and deteriorates after 17 MHz. The best image quality with low RIE and high ICC can be observed from 13 MHz to 17 MHz, where the two curves of the image quality indexes experienced plateau stage.

D. Discussion

The above results and analysis show that the real part and the imaginary part of the impedance tell totally different stories with the frequency change by comparing measurement data, sensitivity distribution and imaging quality in a wide frequency range.

Within the investigated frequency range, low working frequency is preferred for the real part, while relatively high working frequency is preferred for the imaginary part. It is interesting to find that the frequency offering the highest average projection, the best sensitivity distribution and imaging performance for the real part is 1 MHz, rather than the lowest investigated frequency. A possible explanation for this is the existence of the coupling capacitances in CCEIT. Although the coupling capacitance does not exist directly in the real part measurements, they exist as the background signal (noise signal), the SNR will be reduced if the frequency is too low, i.e., the reactance of coupling capacitance will be high at low frequency. So, the 1MHz may be the trade-off point, which is high enough to allow contactless imaging through the pipe, but not too high to be contaminated by the other component of the impedance.

For the imaginary part, although higher frequency is preferred considering from the measurement aspect and the sensitivity aspect, it is surprising to find that the best image quality is at the frequency range of 13 MHz - 17 MHz. The explanation may

be that if the frequency is too high, some limiting factors like skin effect begin to play a visible role. Go back to the measurement value and the sensitivity distribution indexes of the imaginary part in Fig. 7(a) and Fig. 8(b), it can be observed that the measurement value and the sensitivity indexes change more and more slowly as the frequency goes up. After 15 MHz, the changes are very small and the measurement values or the sensitivity indexes obtained at the subsequent frequency points become comparable. So, combining the three aspects, a relatively high frequency of 15 MHz can reconstruct good-quality imaginary part image.

To ensure good imaging performance, 1 MHz and 15 MHz are selected respectively as the working frequencies for the real part and the imaginary part of the impedance. The dual-frequency imaging is then specified at the two working frequencies. That is, to obtain the fused image by fusing the real part image reconstructed at 1 MHz and the imaginary part image reconstructed at 15 MHz.

IV. Verification Experiment and Results

With the experimental setup, verification experiment was carried out to verify the effectiveness of the two optimized working frequencies. Fig. 10 shows the three distribution setups S4 - S6, where again tap water and plastic rods were used as the materials. The target medium in S4 - S6 are respectively a plastic rod with the diameter of 29.5 mm near the boundary, a plastic rod with the diameter of 39.5 mm in the center, and two plastic rods with the diameters of 29.5 mm and 39.5 mm near the boundary.

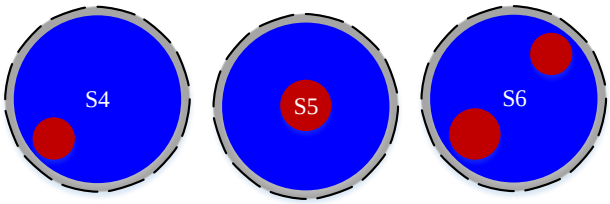

Fig. 10 Distribution setups in verification experiment.

Table II and IV show the imaging results of distribution S4 - S6 respectively, where eight frequencies from 500 kHz to 20 MHz are included. For both the three distributions, the real part images at multiple frequencies indicate that better real part imaging performance can be achieved at low working frequency and again the highest image quality is with the 1 MHz in most cases, although the distribution setups are different from those in the previous frequency selection experiment. The images of the imaginary part at multiple frequencies show that higher working frequency ensures better imaginary part imaging performance, and the images at the very low frequencies even failed to reconstruct the target. And for the imaginary part with the three setups, 15 MHz is always among the best choices.

At each individual frequency, the real part image and the imaginary part image are also fused by pixel-level image fusion. Here, the half-half weighted fusion is applied. With the real part image and the imaginary part image, the *n*th pixel of the fused image G^F is determined as:

$$g_n^F = \frac{1}{2}(g_n^R + g_n^X) \tag{12}$$

where $\tilde{g}_n^R$ is the *n*th pixel in the normalized real part image $\tilde{G}^R$ and $\tilde{g}_n^X$ is the *n*th pixel in the normalized imaginary part image $\tilde{G}^X$.

Fig. 11 shows the image quality indexes of the fused images, including the fused images obtained by single-frequency imaging and the presented dual-frequency imaging with the two optimized frequencies. Compared with the fused images obtained at individual frequencies, the fused image obtained with the dual-frequency idea has higher image quality (smaller relative image error and higher image correlation coefficient), which verifies the effectiveness of the dual-frequency imaging framework and the optimization of the working frequencies.

TABLE II
IMAGING RESULTS OF DISTRIBUTION SETUP S4

f	500k	1M	2M	4M	6 M	9M	12M	15M	18M	20M	Proposed
G^R	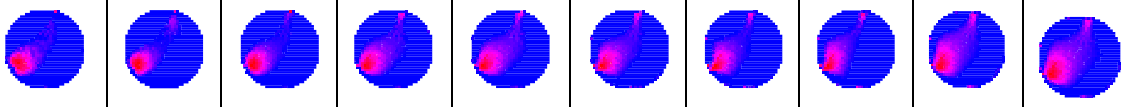										
G^X	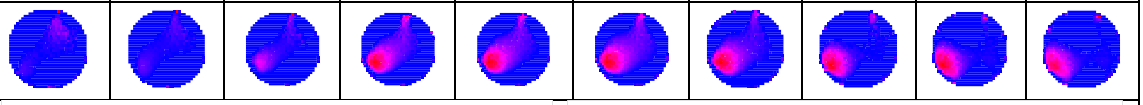										 **1M**
IRE & ICC	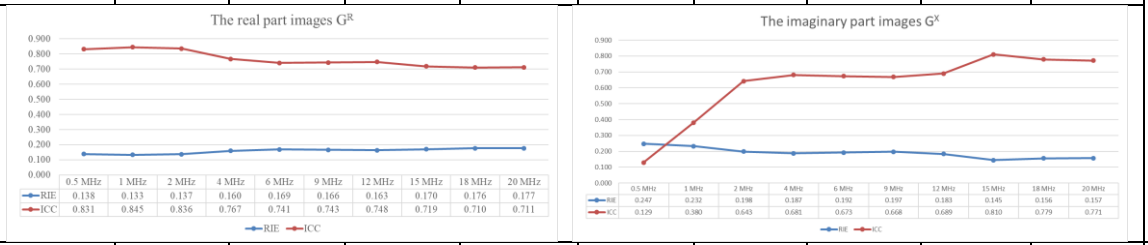										 **15M**
G^F	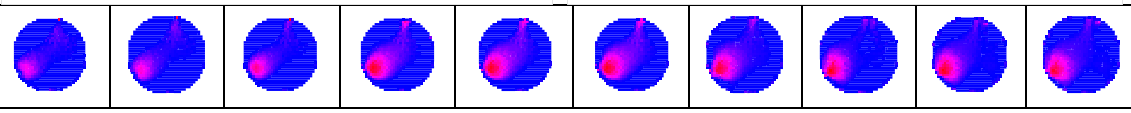										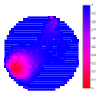

TABLE III
IMAGING RESULTS OF DISTRIBUTION SETUP S5

f	500k	1M	2M	4M	6 M	9M	12M	15M	18M	20M	Proposed
G^R											
G^X											**1M**
IRE & ICC	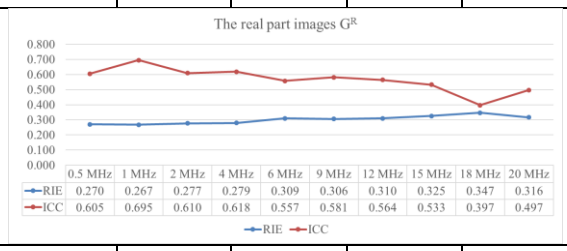					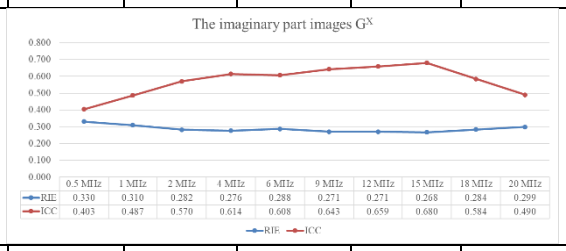					 **15M**
G^F											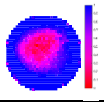

TABLE III
IMAGING RESULTS OF DISTRIBUTION SETUP S6

f	500k	1M	2M	4M	6 M	9M	12M	15M	18M	20M	Proposed
G^R											
G^X											**1M**
RIE & ICC	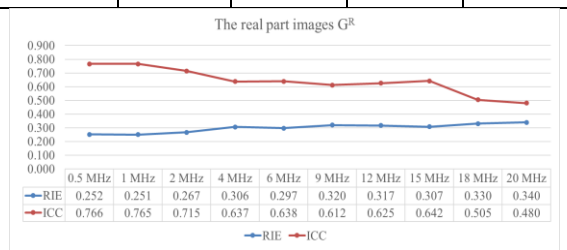					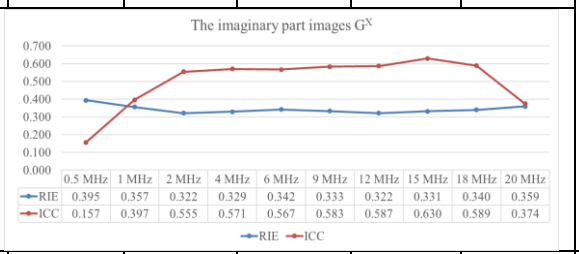					 **15M**
G^F											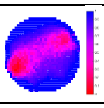

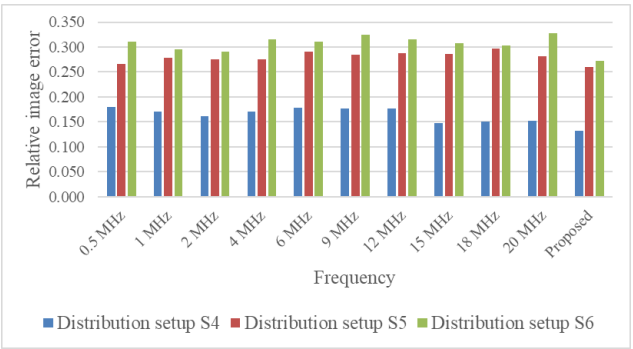

(a)

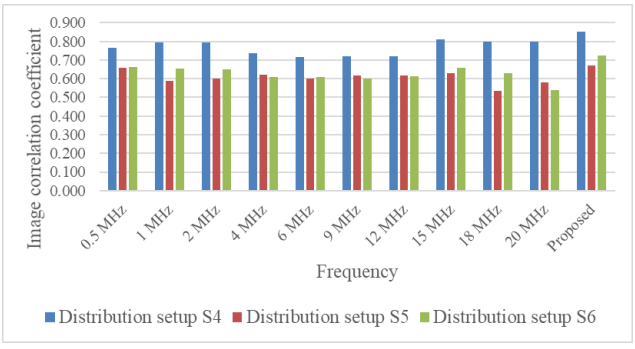

(b)

Fig. 11 Image quality indexes of the fused images: (a) The relative image error; (b) The image correlation coefficient.

V. Conclusion

Based on a new dual-frequency imaging framework, working frequency optimization of CCEIT is implemented in this work. In the new framework, the real part and the imaginary part of the impedance are obtained at two different frequencies for image reconstruction, and the two images are further fused to obtain the fused image. As the key of dual-frequency imaging, the two frequencies for the real part and the imaginary part are optimally selected. This is done by evaluating and comparing the impedance measurement, the sensitivity distribution and the imaging quality of CCEIT in a wide frequency range. From the research results obtained by simulation and experiment, following conclusions can be made:

(1) Preferred working frequency of CCEIT for the real part and the imaginary part of the impedance are totally different. For the real part, a low working frequency is recommended with larger measurement/projection value, better sensitivity distribution and higher image quality. While for the imaginary part, a relatively high frequency is recommended based on the same considerations.

(2) The optimized working frequencies, i.e., 1 MHz for the real part and 15 MHz for the imaginary part, are reasonable. Results of verification experiment show that the 1 MHz for the real part and the 15 MHz for the imaginary part are among the optimal choices in most cases of the tested distribution setups.

(3) The proposed dual-frequency imaging framework is effective. The idea of dual-frequency imaging provides a new approach for improvement of CCEIT. Compared with the fused images obtained at individual frequencies, the fused images obtained by dual-frequency imaging has higher quality, which means that dual-frequency imaging takes better advantage of the impedance information.

Compared to the single-frequency imaging, dual-frequency imaging gives the whole image of the real part and imaginary part, rather than image of single component. Compared with multifrequency imaging, the dual-frequency has much higher efficiency because multifrequency imaging needs long data collection and image reconstruction time.

Useful knowledge and experience concerning multi-spectral CCEIT have been obtained, which provides a good reference for further development of CCEIT. As the very preliminary research of CCEIT with multi-frequency imaging, more interesting work will be undertaken in the future. For example, seeking/proposing more suitable image reconstruction algorithm and image fusion algorithm for the dual-frequency CCEIT. Addressing the dual-frequency idea with specific applications where the multi-spectral impedance characteristics of the specific medium will be revealed to give guidance for specific frequency optimization and parameter measurement. In future work it is also possible to expand the idea of dual-frequency imaging to include more workable frequencies or even extend the frequency ranges, etc.

References

[1] D. S. Holder, Electrical Impedance Tomography: Methods, History and Applications, IOP Publishing, 2005.

[2] Wang M, Industrial Tomography - Systems and Applications, Elsevier, 2015.

[3] Y. Wahab and R. Rahim, “Non-invasive process tomography in chemical mixtures—A review,” Sens. Actuators B Chem., vol. 210, pp. 602–617, 2015.

[4] L. Borcea. “Electrical impedance tomography”. Inverse problems. vol. 18, no. 6, pp. R99-R136, 2002.

[5] B. H. Brown, “Medical impedance tomography and process impedance tomography: A brief review," Meas. Sci. Technol., vol. 12, no. 8, pp. 991-996, 2001.

[6] Y. A. Wahab, R. A. Rahim, L. P. Ling, et al., “Optimisation of electrode dimensions of ERT for non-invasive measurement applied for static liquid-gas regime identification,” Sens. Actuators A, phys., vol. 270, pp. 50-64, 2018.

[7] P. Newwill, D. Karadaglic, F. Podd, et al., “Electrical impedance imaging of water distribution in the root zone,” Meas. Sci. Technol., vol. 25, 2014, Art. no. 055110.

[8] J. T. Sun and W. Q. Yang, “Fringe effect of electrical capacitance and resistance tomography sensors,” Meas. Sci. Technol., vol. 24, 2013, Art. no. 074002.

[9] A. McEwan, G. Cusick and D. S. Holder, “A review of errors in multi-frequency EIT instrumentation,” Physiol. Meas., vol. 28, no. 7, pp. 197-215, 2007.

[10] V. Kolehmainen, M. Lassas and P. Ola, “Electrical impedance tomography problem with inaccurately known boundary and contact impedances,” IEEE Trans. Med. Imag., vol. 27, no. 10, pp. 1404-1414, 2008.

[11] Y. Wang, H. Ji, Z. Huang, et al., “Study on image reconstruction of capacitively coupled electrical impedance tomography (CCEIT),” Meas. Sci. Technol., vol. 30, no. 9, Jul. 2019, Art. no. 094002.

[12] X. K. He, Y. D. Jiang, B. L. Wang, et al., “An Image Reconstruction Method of Capacitively Coupled Electrical Impedance Tomography (CCEIT) Based on DBSCAN and Image Fusion,” IEEE Trans. Instrum. Meas., vol. 70, 2021, Art. no. 4503111.

[13] E. Barsoukov, R. J. Macdonald. Impedance Spectroscopy: Theory, Experiment, and Applications. Wiley-Interscience, 2005.

[14] M. M. Zhang, M. Soleimani. “Simultaneous reconstruction of permittivity and conductivity using multi-frequency admittance measurement in electrical capacitance tomography,” Meas. Sci. Technol., vol. 27, no. 2, 2016, Art. no. 025405.

[15] J. T. Sun, W. Q. Yang. “A dual-modality electrical tomography sensor for measurement of gas–oil–water stratified flows,” Measurement, vol. 66, pp. 150-160, 2015.

[16] Y. J. Yang, J. B. Jia, “A multi-frequency electrical impedance tomography system for real-time 2D and 3D imaging,” Rev. Sci. Instrum., vol. 88, no. 8, 2017, Art. no. 085110.

[17] M. M. Zhang, L. Y. Zhu, H. K. Wang, et al., “Multiple Measurement Vector-Based Complex-Valued Multifrequency ECT,” IEEE Trans. Instrum. Meas., vol. 70, 2021, Art. no. 5005410.

[18] E. Malone, G. S. D. Santos, D. Holder, and S. Arridge, “Multifrequency Electrical Impedance Tomography Using Spectral Constraints,” IEEE Trans. Med. Imag., vol. 33, no. 2, pp. 340–350, 2014.

[19] W. R. B. Lionheart, “EIT reconstruction algorithms: pitfalls, challenges and recent developments,” Phys. Meas., vol. 25, no. 1, pp. 125-142, 2004.

[20] W. Q. Yang, L. H. Peng, “Image reconstruction algorithms for electrical capacitance tomography,” Meas. Sci. Technol., vol. 14, pp. R1-R13, 2003.

[21] Z. Q. Cui, Q. Wang, Q. Xue, et al., “A review on image reconstruction algorithms for electrical capacitance/resistance tomography,” Sensor Rev., vol. 36, no. 4, pp. 429–445, 2016.

[22] H. B. Mitchell, Image Fusion: Theories, Techniques and Applications, Springer, 2010.

[23] K. Brandisky, D. Sankowski, R. Banasiak, et al., “ECT sensor optimization based on RSM and GA,” The International Journal for Computation & Mathematics in Electrical & Electronic Engineering (Compel), vol. 31, no. 3, pp. 858-869, 2012.

[24] Z. Xu, Y. D. Jiang, B. L. Wang, et al. “Image Reconstruction Performance of a 12-Electrode CCERT Sensor under Five Different Excitation Patterns,” IEEE Access, vol. 6, pp. 65783-65795, 2018.

[25] Z. Wang, A. C. Bovik, H. R. Sheikh, et al., “Image quality assessment: From error visibility to structural similarity,” IEEE Trans. Image Process., vol. 13, no. 4, pp. 600–612, 2004.